Electronic Supplementary Material (ESI) for Energy & Environmental Science.

A Bottom-up Understanding of the Ligand-dominated Formation of Metallic Nanoparticle Electrodes with High Broadband Reflectance Enable Fully Solution-processed Large-area Organic Solar Cells

Jiawei Zheng[1], Xinjun He[1], Yuniu Zhang[1], Benzheng Lyu[1], Jinwook Kim[1], Shiang Li[3], Xinhui Lu[3], Haibin Su[2], Wallace C.H. Choy[1]**

[1]Department of Electrical and Electronic Engineering, the University of Hong Kong, Pok Fu Lam Road, Hong Kong SAR, China

[2]Department of Chemistry, the Hong Kong University of Science and Technology, Clear Water Bay, Hong Kong SAR, China

[3]Department of Physics, the Chinese University of Hong Kong, Central Ave, Hong Kong SAR, China

Email address: chchoy@eee.hku.hk; haibinsu@ust.hk

Gallic acid-assisted synthesis of AgNPs and characterizations

The silver nanoparticles are synthesized by a room-temperature process, as shown in **Figure S1a**. Silver acetate dihydrate ($AgAC \cdot 2H_2O$) is selected as the Ag source, dispersed in methanol. Gallic acid (GA) is employed as the reductant and stabilizer in this system. A detailed description of the synthesis process can be found in the experimental section. The reaction mechanism can be dispersed as follows:

$$\mathrm{Ag^+ + GA^- \rightarrow Ag\text{-}GA}, \tag{S1}$$

$$\mathrm{NBA + MeOH \rightarrow NBAH^+ + MeO^-}, \tag{S2}$$

$$\mathrm{GA(C\text{-}OH)\ (reductant) + Ag\text{-}GA + MeO^- \rightarrow GA(C{=}O) + Ag\downarrow + MeOH + GA^-}, \tag{S3}$$

$$\mathrm{NBAH^+ + GA^- \rightarrow NBA + GA}. \tag{S4}$$

When GA is added to the Ag-source solution, it can quickly connect to the Ag^+ (shown in **equation S1**) and make the dispersion uniform. The NBA acts as a catalyst for accelerating the reaction[S1]. In **equation S3**, the hydroxy in GA can reduce the Ag^+ and generate Ag particles. Finally, the GA(COOH) will become the stabilized ligands at the surface of Ag nanoparticles due to the interaction between -COOH and Ag. The amount of the GA will significantly influence the particle size distributions and the storage stability of the products. Two different amounts of GA-based AgNPs (named GA*1 and GA*3) are applied to analyze the influence. **Figure S1b, c** show the SEM images and the particle size distribution of the AgNP films of GA*1 and GA*3. It can be found that a large amount of GA can significantly change the particle size distribution. GA*3 presents a slightly smaller average particle size (45.7 nm) than GA*1 (51.4 nm). However, the standard deviations of particle sizes for GA*1 and GA*3 are 21.1 nm and 13.2 nm, indicating that the size distribution of GA*3 is much more uniform than GA*1. The possible mechanism of the distribution change is that large amounts of GA ligand in the solution could mix well with the Ag source at the beginning of the reaction. All the Ag sources reduce at a similar rate and stop growing at a similar period because of the high intensity of stabilized ligands. In contrast, the lack of GA may lead to the isolated Ag source, which can react quickly and aggregate to a large particle. Moreover, the lack of GA ligand in the final products contributes to poor storage stability, as shown in **Figure S1d**. After low-temperature storage for 30 days, the particle size distribution of GA*1 significantly changed. The average size of AgNPs almost doubled, and the largest particle reached 170 nm, which is adverse for film deposition. The GA*3 showed superior storage stability and almost consistent size distribution after 30 days. The respective distribution diagrams for GA*1 and GA*3 at different periods are presented in **Figure S2**. In conclusion, sufficient GA ligands in the synthesis process can help to control the reaction speed and achieve particles of uniform size. It also improves the storage stability of AgNPs, benefiting from the stabilizer effects of GA. Good storage stability is an indispensable part of the nanoparticle for commercial applications. In the rest of this work, all the characterizations and applications are based on GA*3 silver nanoparticles (AgNP-GA). The surface charge of the particles is almost neutral, and the Zeta potential of the AgNP-GA at 25 °C is -10.37 mV as shown in **Figure S3**.

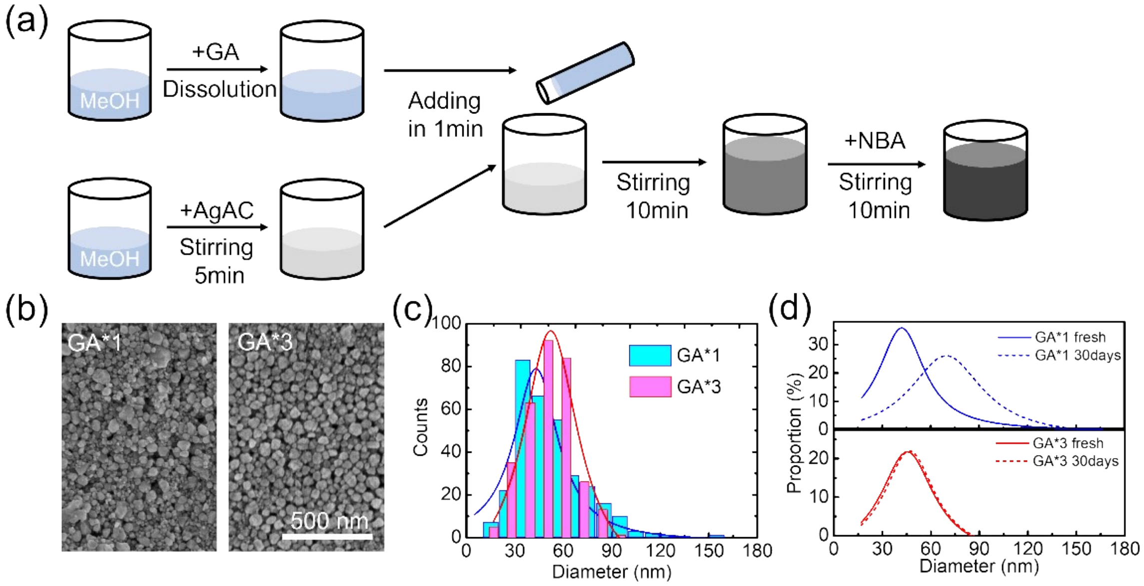

Figure S1 a) The schematic diagram of the synthesis process of silver nanoparticles at room temperature. b) The SEM images for GA*1 and GA*3 films. The scale bar is 500 nm. c) The particle diameter distribution of GA*1 and GA*3. The dash histograms are counted numbers, and the lines are fitted distribution curves. d) The fitted particle diameter distribution for fresh AgNPs and AgNPs after 30 days of storage.

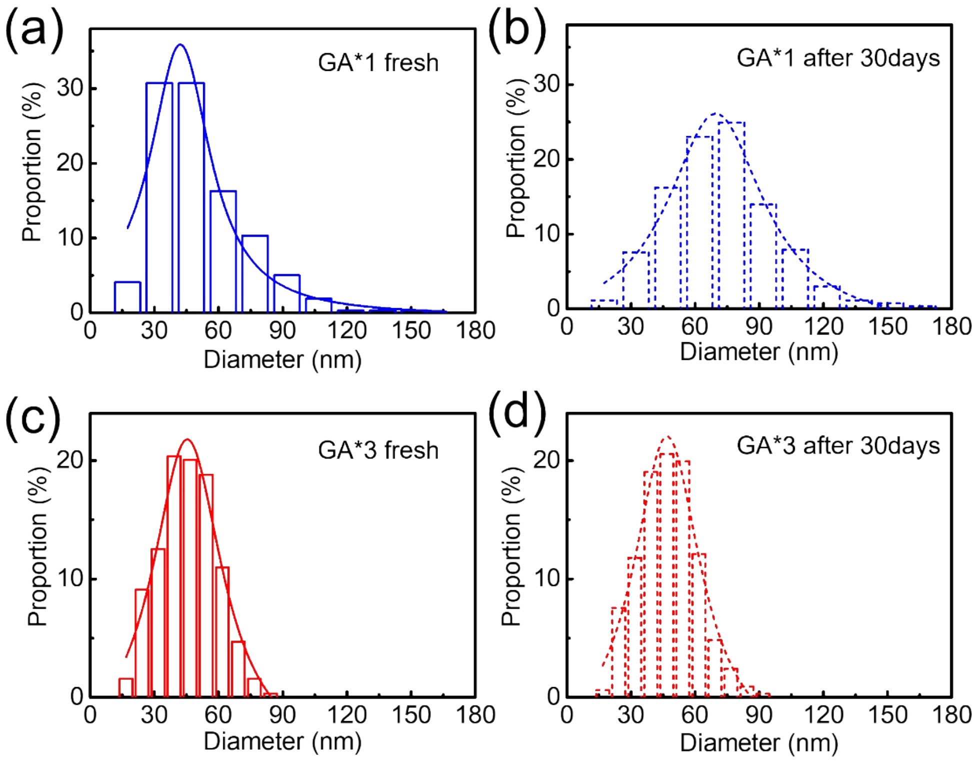

Figure S2 The respective distribution diagrams for a) fresh GA*1, b) GA*1 after 30 days of storage, c) fresh GA*3, and d) GA*3 after 30 days of storage. The histograms are calculated proportions, and the lines are fitted distribution curves.

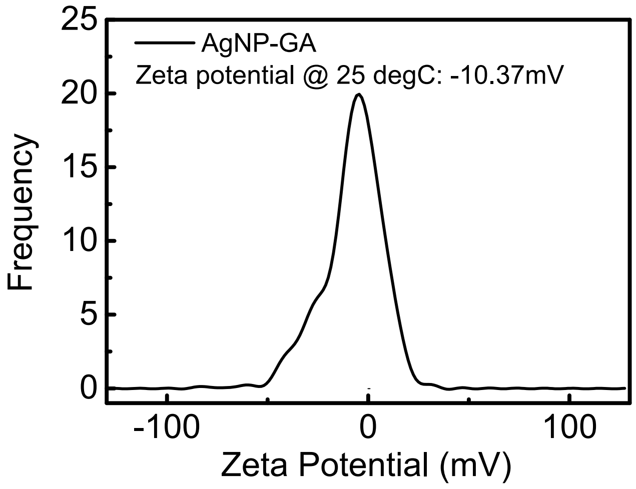

Figure S3 Zeta potential of AgNP-GA at 25 °C.

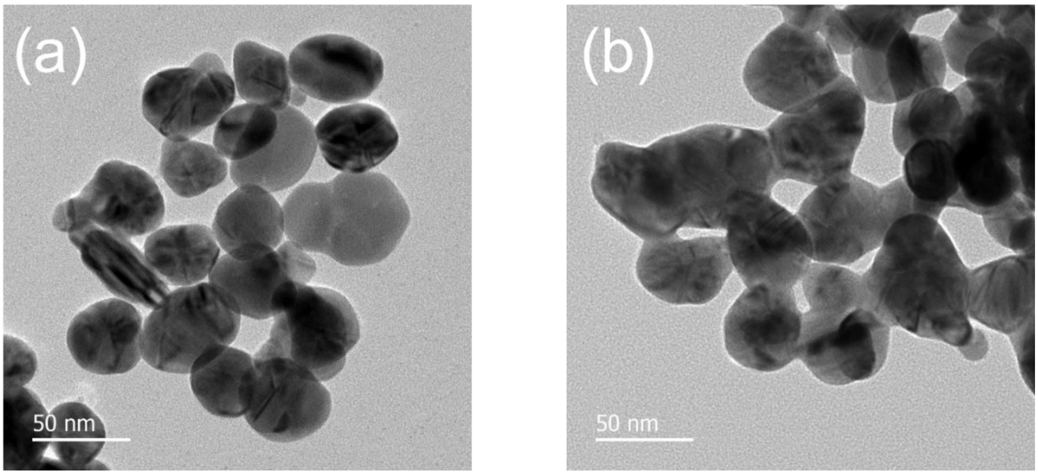

Figure S4 TEM images of AgNPs a) before and b) after annealing with a scale bar of 50 nm.

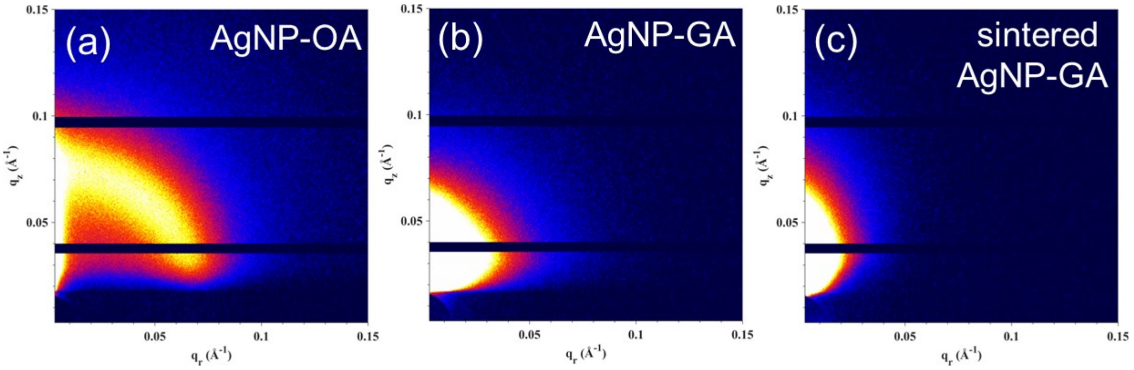

Figure S5 Grazing-Incidence Small-Angle X-ray Scattering (GISAXS) images of AgNP thin films: a) AgNP-OA; b) AgNP-GA; and c) sintered AgNP-GA.

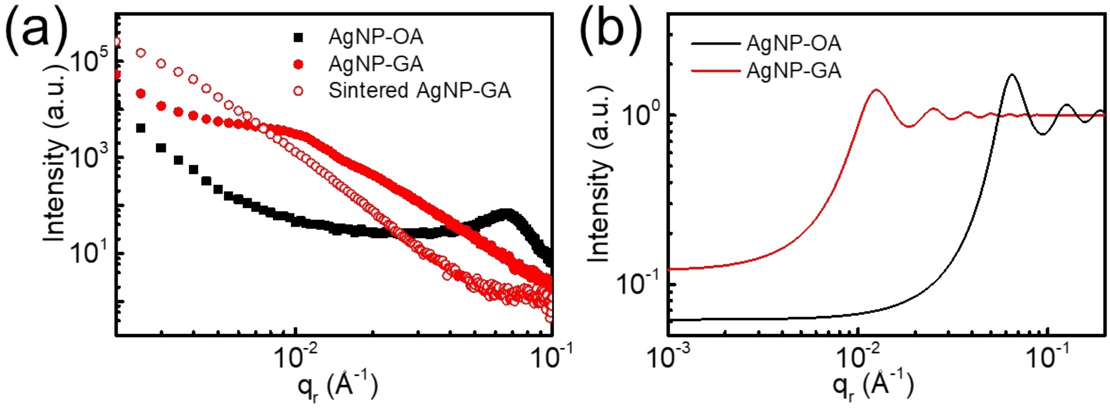

Figure S6 a) GASAXS data of AgNP-OA and AgNP-GA before and after sintering. b) structure factor of AgNP-OA and AgNP-GA.

From the 2D plots of the GISAXS in **Figure S5a, b**, it is clear that the nanoparticles with GA as the ligand show a random packing status while the one with OA packs more orderly, representing by the appearance of a ring-like pattern in GISAXS**.** We also obtain the intensity profile along the q_r direction as shown in **Figure S6a**. The main feature of AgNP-GA is located at q_r around 0.012 Å^{-1}. The feature of AgNP-OA is located at 0.065 Å^{-1}, roughly corresponding to the particle size measured via TEM.

$$particle\ radius\ in\ \text{Å} \approx \frac{2\pi}{qr\ value\ of\ main\ feature}$$

Assuming there are a hard sphere interactions between Ag nanoparticles, the interparticle potential is:

$$U(r) = \begin{cases} \infty & r < 2R \\ 0 & r \geq 2R \end{cases}$$

From the intensity profile in **Figure S6b**, we can get the structure factor $S(q)$. The interparticle distance can be calculated via the following formula:

$$Interparticle\ distance\ \frac{2\pi}{q\ value\ of\ main\ peak} - diameter$$

The determined interparticle distances are 3.1nm for AgNP-OA and 0.2 nm for AgNP-GA.

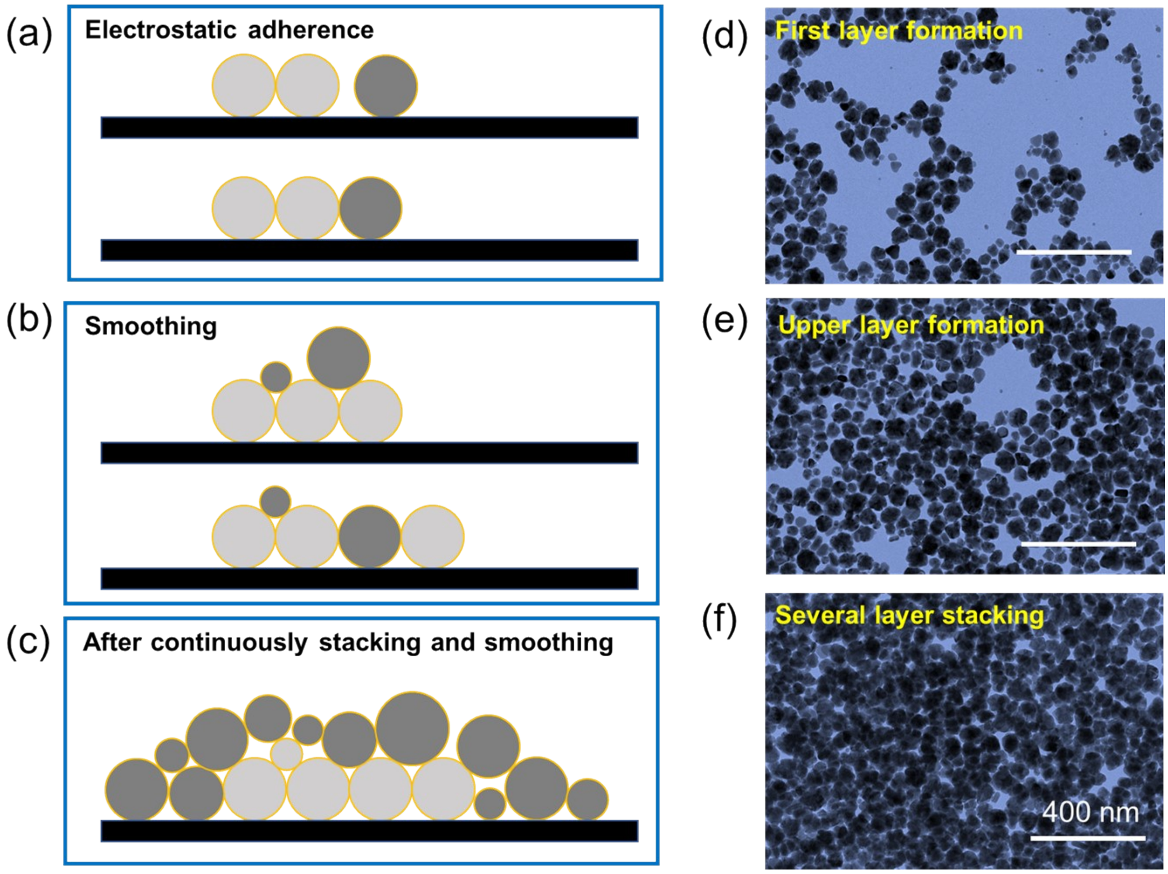

Figure S7 The schematic diagrams of the particle stacking procedures including a) electrostatic adherence, b) smoothing steps, and c) stacked condition after continuously stacking and smoothing. The TEM images of stacking conditions of AgNP-GA after d)1 cycle; e) 2 cycles; and f) 4 cycles.

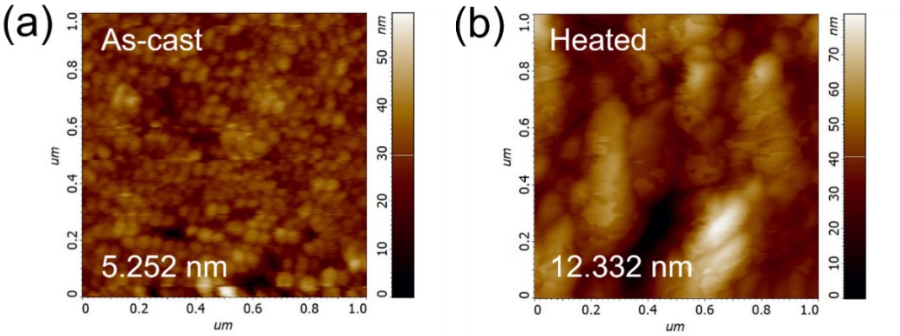

Figure S8 AFM images of AgNPs a) before and b) after annealing with an area of 1 μm × 1 μm. The RMSs of the films are marked in the images.

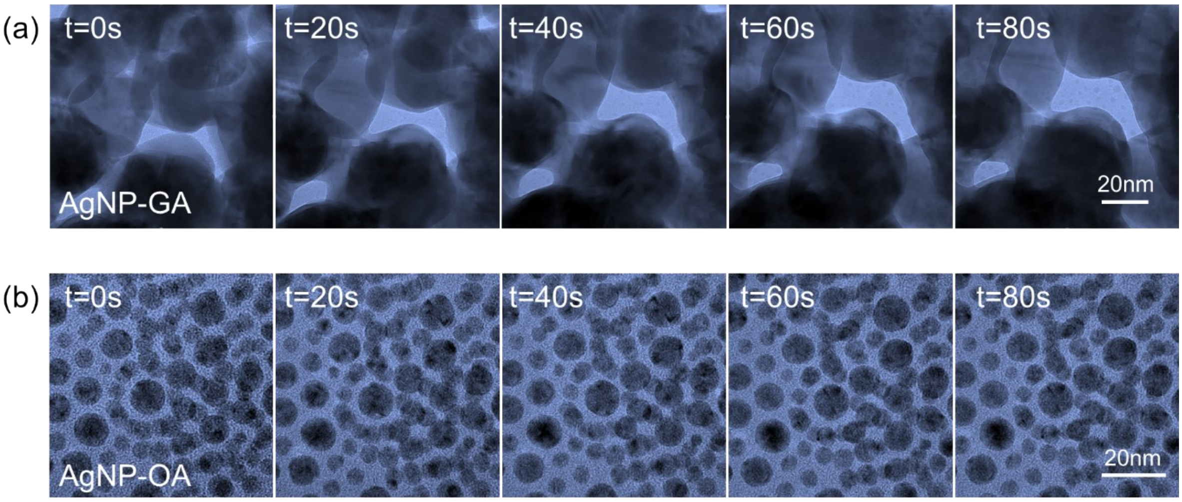

Figure S9 The time-varying TEM of a) AgNP-GA and b) AgNP-OA.

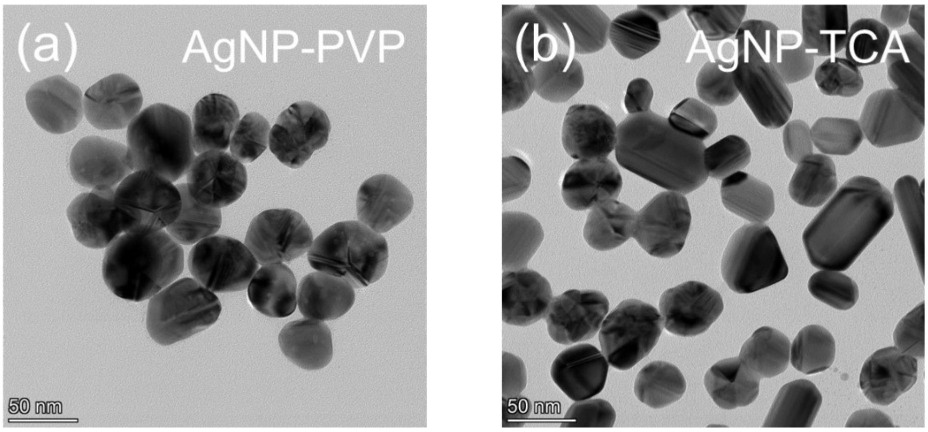

Figure S10 TEM images of a) AgNP-PVP and b) AgNP-TCA. The average particle size of both cases is around 50 nm.

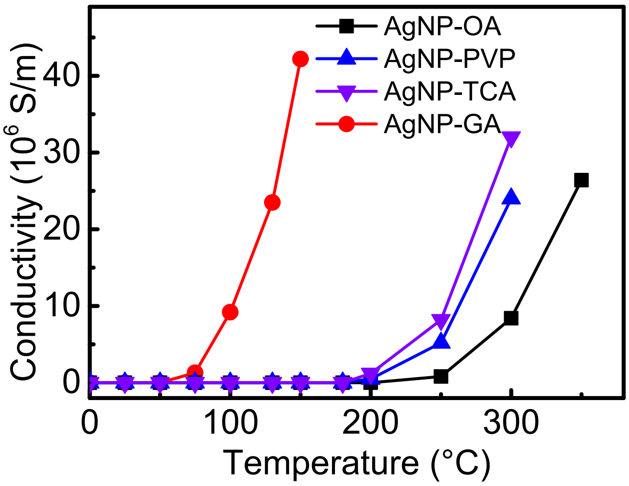

Figure S11 The conductivity-temperature curves of AgNPs thin films.

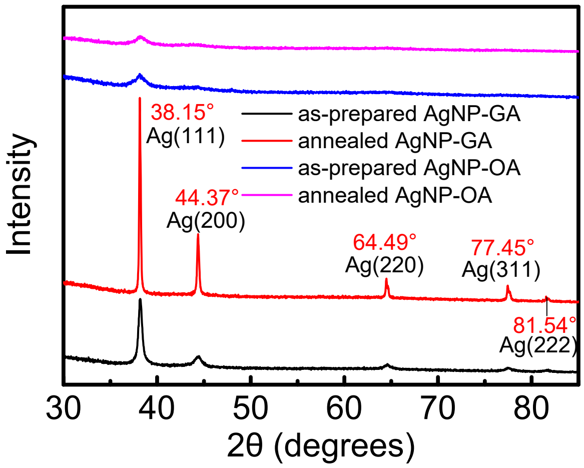

Figure S12 XRD of AgNP-OA and AgNP-GA thin films before and after annealing at 130°C for 5 min.

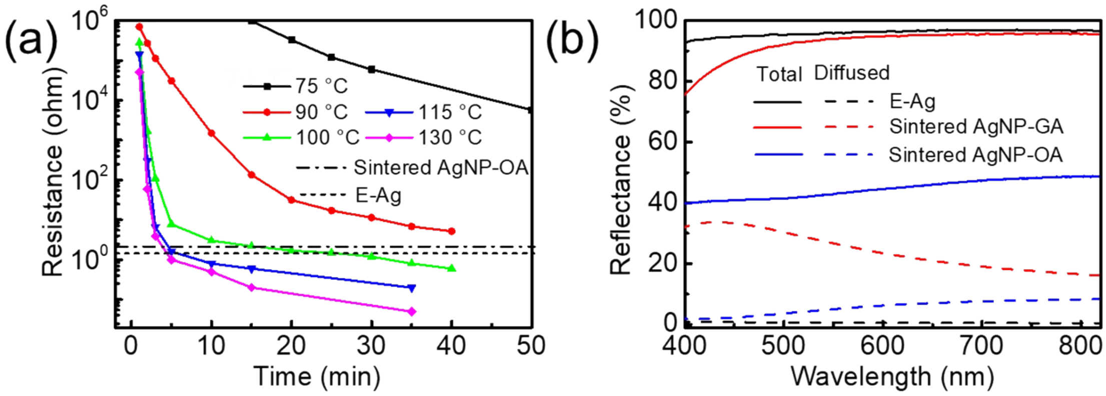

Figure S13 a) The resistance evolution of AgNP-GA films annealed at stepwise temperatures. The dash lines represent the resistances of sintered AgNP-OA film and evaporated Ag (E-Ag) thin film. b) The total (solid lines) and diffused (dash lines) reflectance spectrum of evaporated Ag (E-Ag), sintered AgNP-GA, and sintered AgNP-OA films.

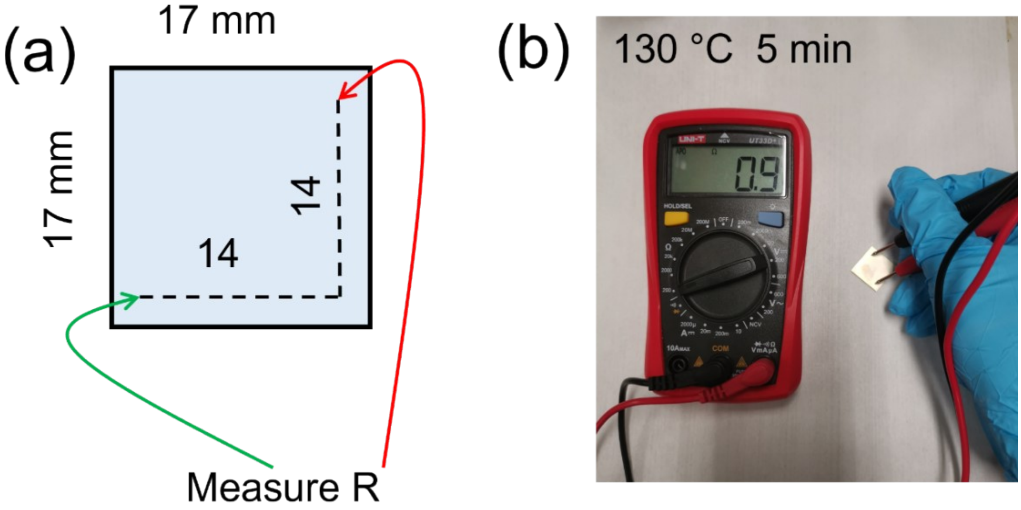

Figure S14 a) The schematic diagram of the resistance measurement. The film is deposited on the 17 mm × 17 mm glass substrates, and the resistance is measured diagonally in a 14 mm × 14 mm square area by a multimeter. b) A natural photograph of the resistance measurement. The AgNP film is annealed at 130 °C for 5 min.

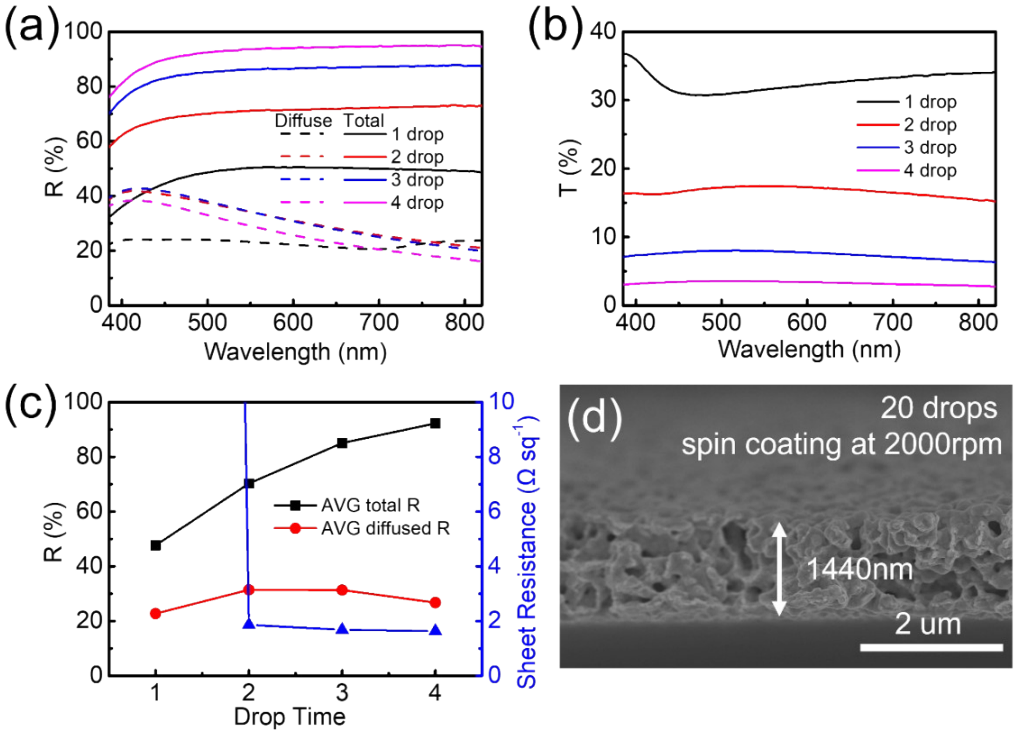

Figure S15 a) The total and diffuse reflectance and b) transmittance spectra of AgNP films with different thicknesses contributed by the drops of solution in the spin-coating process. c) The statistic diagram of the average reflectance and the corresponding sheet resistance of AgNP films with different thicknesses. d) The cross-section SEM of the AgNP film prepared with 20 drops of solution in the coating process.

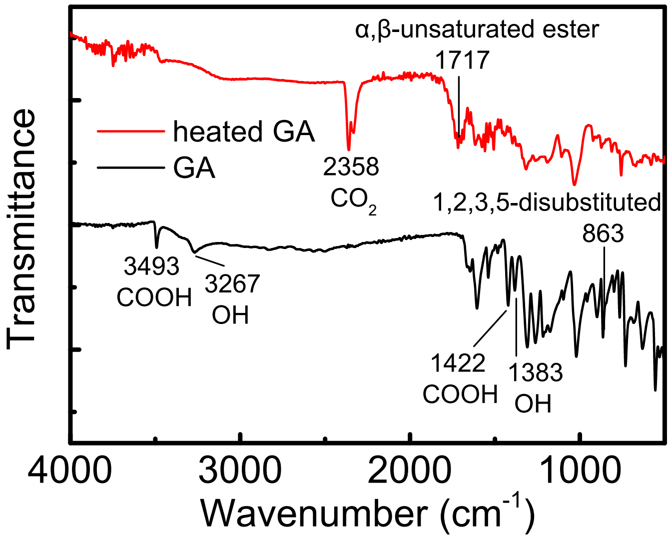

Figure S16 FTIR spectra of GA powers before and after the annealing in a humid environment.

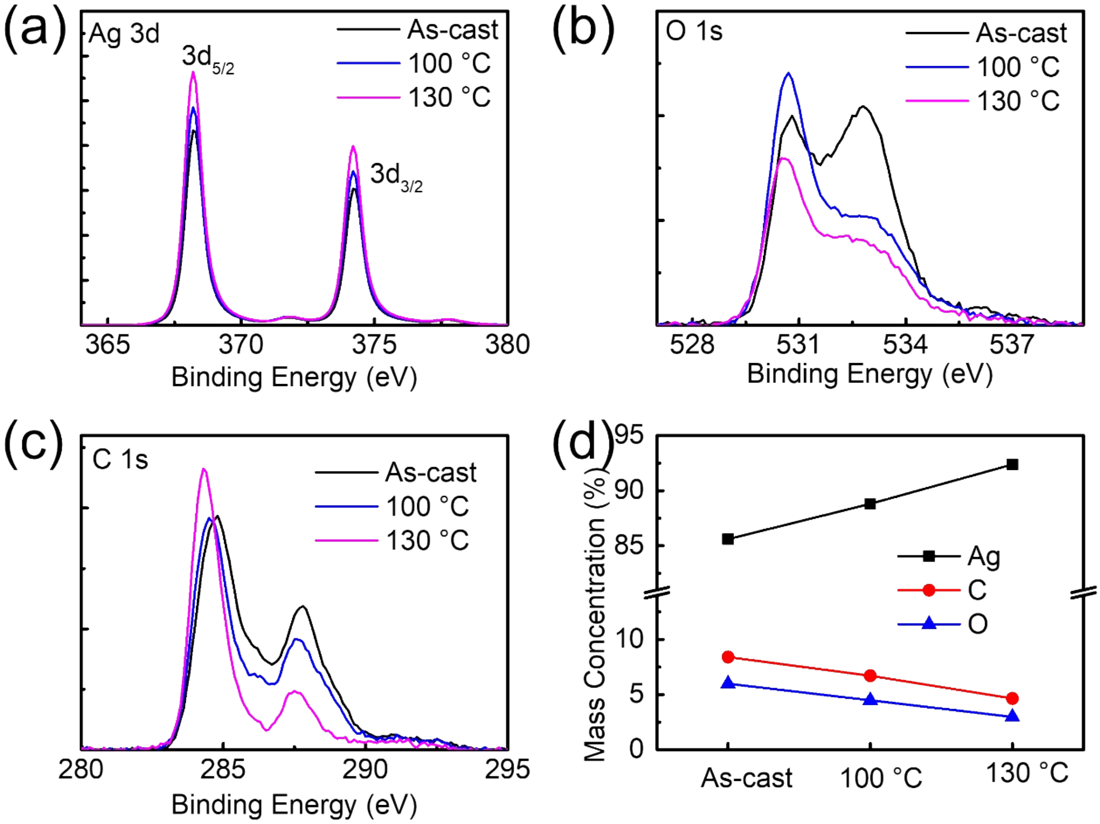

Figure S17 a) Ag 3d, b) O 1s, and c) C 1s XPS spectra of AgNP films before and after the annealing process at 100 °C and 130 °C for 15 min. d) The Ag, C, and O mass concentration of AgNP films before and after the annealing process.

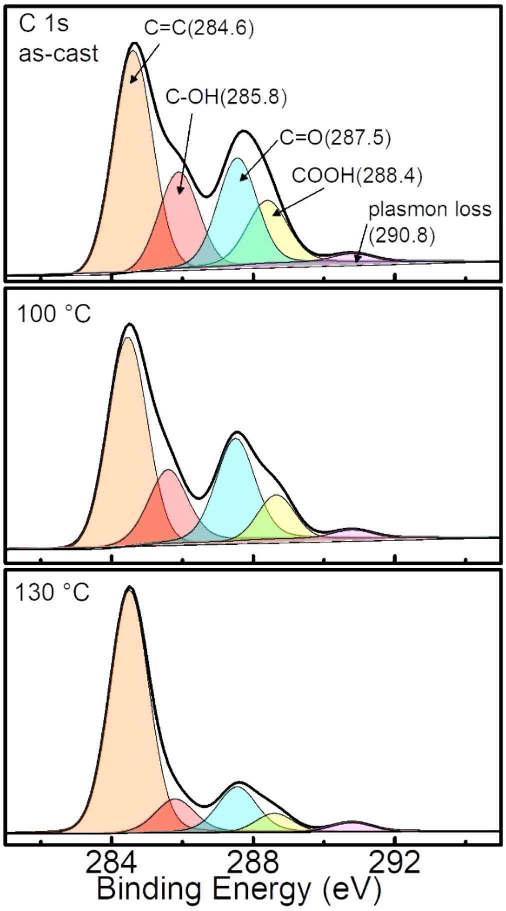

Figure S18 C 1s core-level spectra of AgNP films before and after annealing at 100 °C and 130 °C for 15 min. The relevant peak data are marked in the spectra.

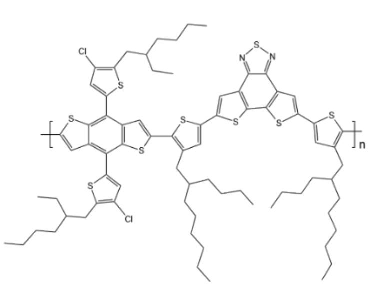

D18-Cl

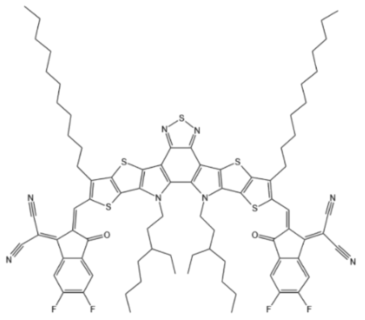

N3

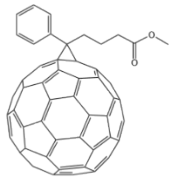

$PC_{61}BM$

Figure S19 The illustrative structure diagrams of D18-Cl, N3, and $PC_{61}BM$.

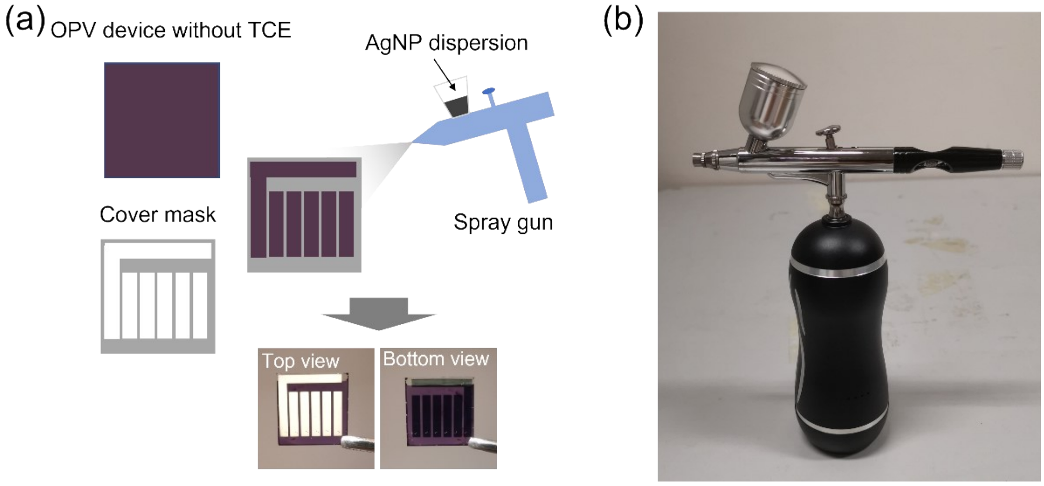

Figure S20 a) The schematic diagram of spray coating AgNPs. The pattern of rear electrodes is introduced by a patterned cover mask. The below photograph is the top and bottom view of the real OSC device. b) The photograph of the portable spray gun with an electrical air pump (black).

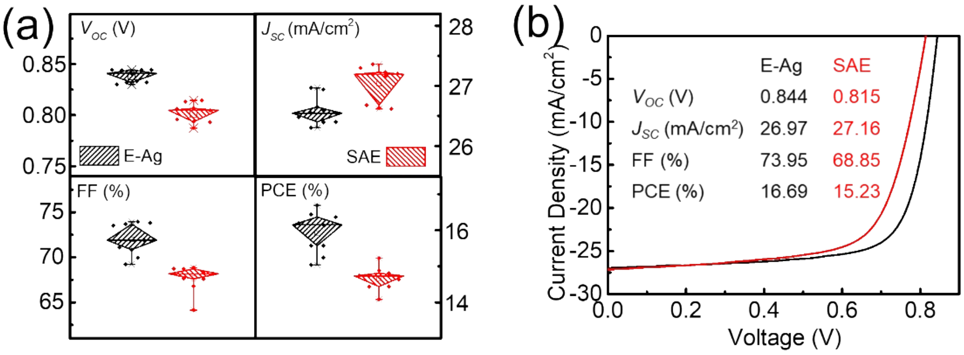

Figure S21 a) The statistical characteristics of the OSC devices (0.08 cm^2) measured with AM 1.5G. b) The ° characteristics of champion devices with evaporated Ag (E-Ag) and SAE.

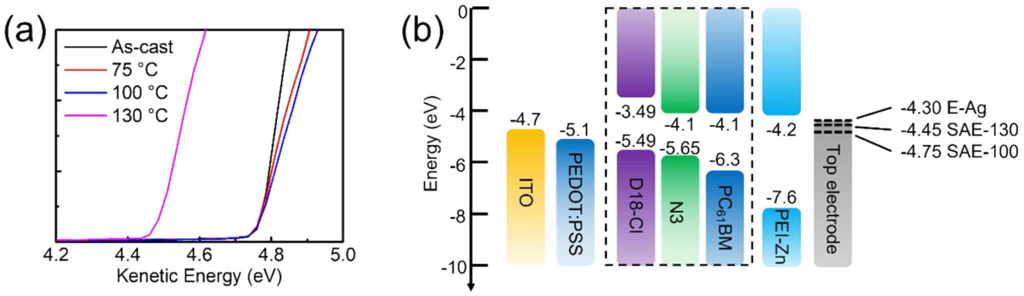

Figure S22 a) UPS spectra of AgNP films before and after the annealing process at 75 °C, 100 °C, and 130 °C. b) The schematic energy diagram of the OSC device with different rear electrodes.

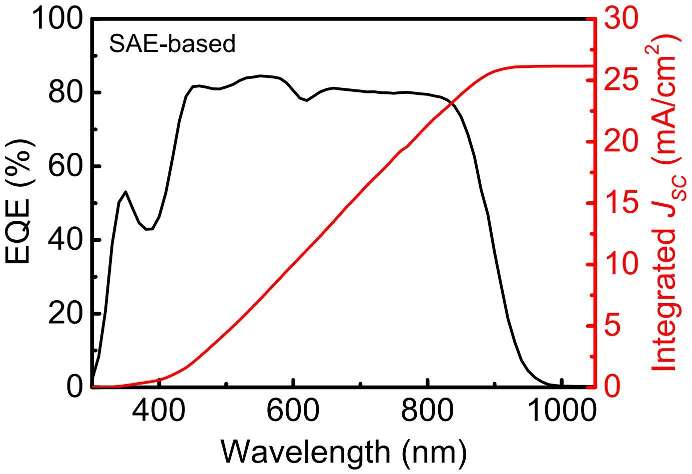

Figure S23 The EQE spectrum and the corresponding integrated J_{SC} of the SAE-based OSCs. The integrated J_{SC} is 26.17 mA/cm^2.

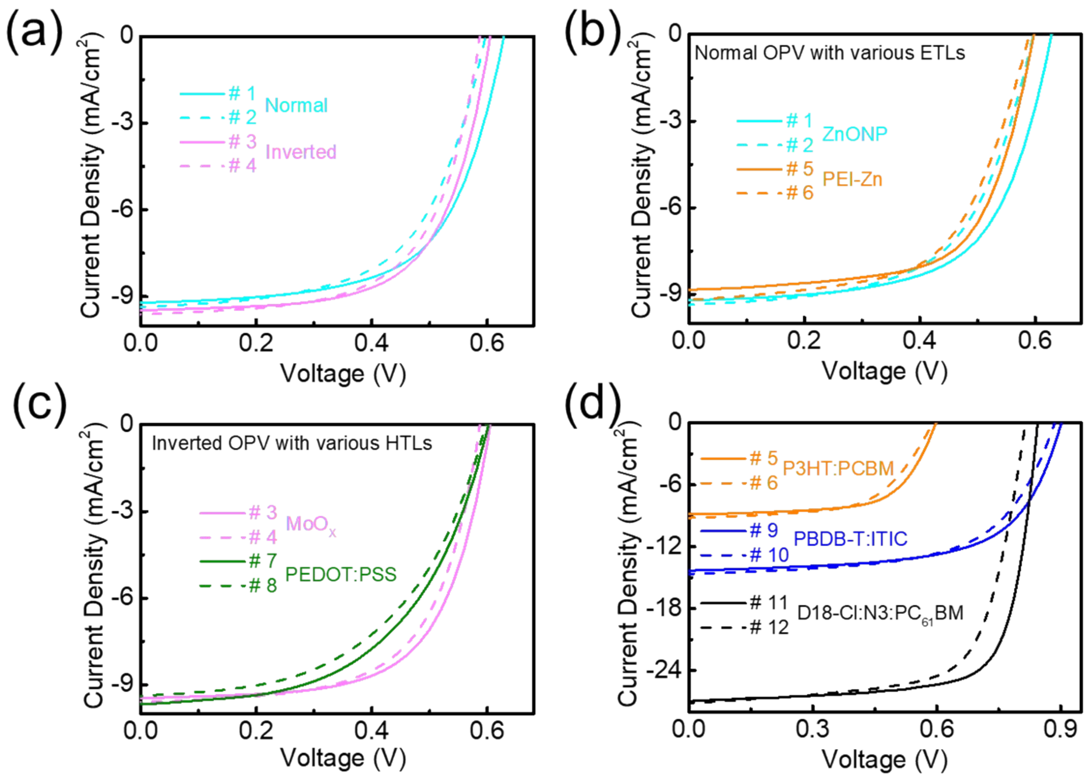

Figure S24 The universal application of AgNP-GA electrode on various structures of OSCs. The solid lines represent devices with evaporated Ag electrodes and dash lines represent devices with AgNP-GA electrodes. a) Comparison of normal and inverted device structure; b) comparison of normal device structures with various ETLs; c) comparison of inverted devices with various ETLs; d) comparison of devices with various active layers. The detailed device structures and performance parameters are listed in **Table S4**

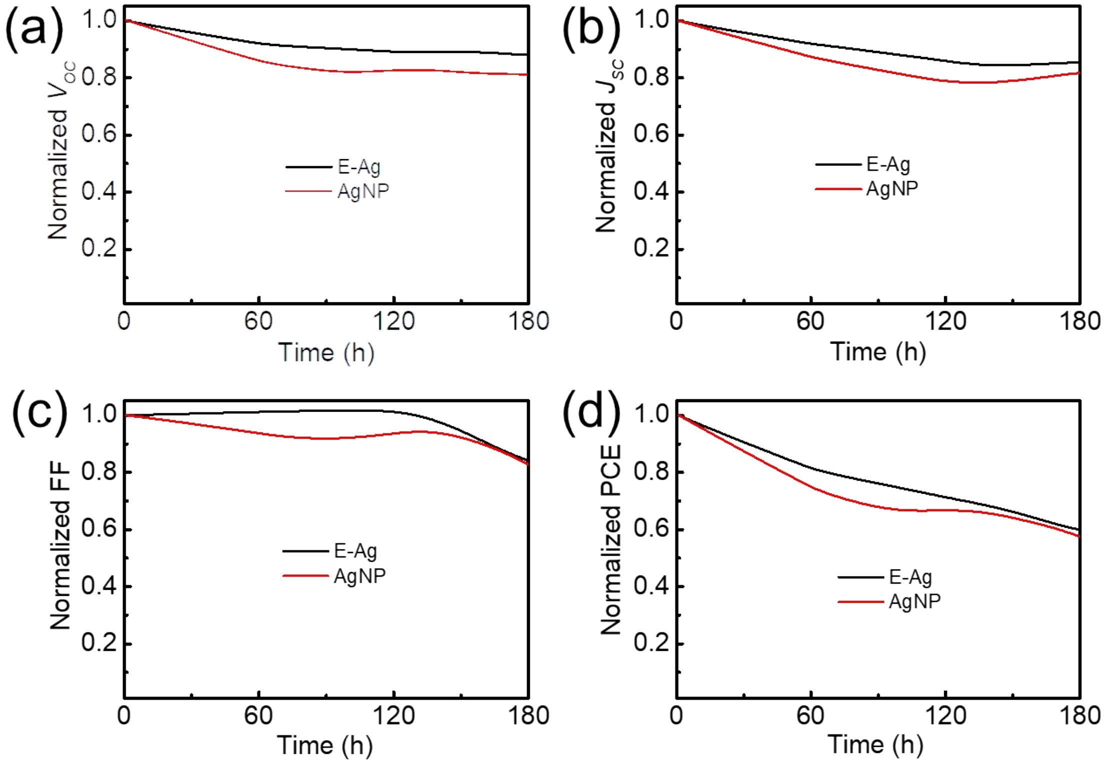

Figure S25 MPP tracking stability of ITO/ PEDOT:PSS/ P3HT:PCBM/ PEI-Zn/ Evaporated Ag (E-Ag) or AgNP devices at air condition (T= 30 °C; RH= 60%), a) V_{OC}; b) J_{SC}; c) FF; and d) PCE.

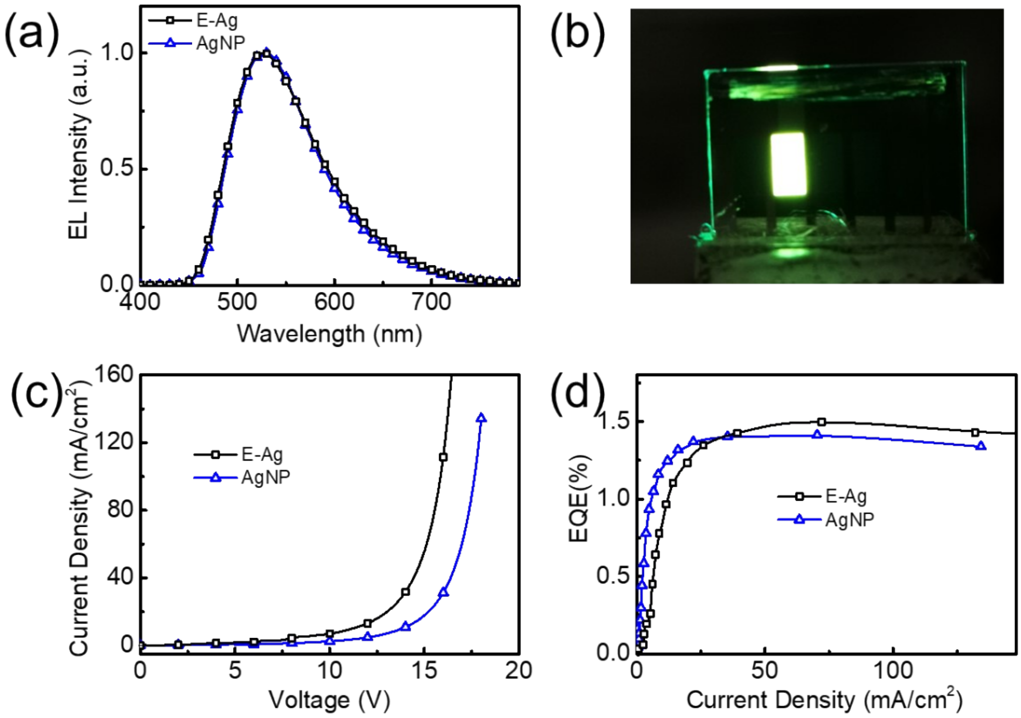

Figure S26 a) EL spectra of organic LEDs with evaporated Ag (E-Ag) and AgNP-GA electrodes. b) The photograph of the device with the AgNP-GA electrode. c) *J*-*V* and d) EQE-*J* characteristics of OLED devices with evaporated Ag (E-Ag) and AgNP-GA electrodes.

Table S1 The statistical data of the mass concentrations of the Ag, C, and O elements in AgNP films before and after the annealing process.

	As-cast	100 °C	130 °C
Ag (%)	85.60	88.80	92.37
C (%)	8.41	6.71	4.65
O (%)	5.99	4.49	2.98

Table S2 The statistical characteristics of the OSC devices with evaporated Ag (E-Ag) and SAE measured with AM 1.5G. The device area is 0.08 cm^2.

	V_{OC} (V)	J_{SC} (mA/cm^2)	FF (%)	PCE (%)
E-Ag (Avg)	0.838	26.59	72.00	15.92
E-Ag (Champion)	0.844	26.97	73.95	16.69
SAE (Avg)	0.802	27.04	67.66	14.67
SAE (Champion)	0.815	27.16	68.85	15.23

Table S3 The review of the large-area OSCs with solution-processed electrodes.

No.	Year	Top electrode	PCE (%)	area (cm^2)
1[S2]	2015	AgNW	2.25	1.6
2[S3]	2015	Ag ink	4.5	12.72*9
3[S4]	2016	PEDOT:PSS/AgNW	5.9	1
4[S5]	2017	PEDOT:PSS/AgNW	4.5	1.04
5[S6]	2018	AgNW	5	5.33*12
6[S7]	2018	PEDOT:PSS	6.65	2.03
7[S8]	2018	PEDOT:PSS	7.6	2.03
8[S9]	2019	PEDOT:PSS	4.81	1
9[S10]	2020	PEDOT:PSS	10.3	1
This work	**2022**	**AgNPs**	**14.69**	**1**

Table S4 A summary of device structures and performance parameters of various OSCs made from AgNP-GA electrodes and evaporated Ag (E-Ag) electrodes.

No.	Device Structure	V_{OC} (V)	J_{SC} (mA/cm^2)	Fill Factor (%)	Efficiency (%)
#1	ITO/ PEDOT:PSS/ P3HT:PCBM/ ZnONP/ E-Ag	0.628	9.21	62.20	3.60
#2	ITO/ PEDOT:PSS/ P3HT:PCBM/ ZnONP/ AgNP	0.597	9.36	59.14	3.31
#3	ITO/ ZnO s-g/ P3HT:PCBM/ MoO/ E-Ag	0.605	9.47	64.17	3.68
#4	ITO/ ZnO s-g/ P3HT:PCBM/ MoO/ AgNP	0.587	9.61	62.45	3.52
#5	ITO/ PEDOT:PSS/ P3HT:PCBM/ PEI-Zn/ E-Ag	0.598	8.84	64.95	3.43
#6	ITO/ PEDOT:PSS/ P3HT:PCBM/ PEI-Zn/ AgNP	0.590	9.19	59.71	3.24
#7	ITO/ ZnO s-g/ P3HT:PCBM/ PEDOT:PSS (0.5% triton)/ E-Ag	0.602	9.68	53.47	3.11
#8	ITO/ ZnO s-g/ P3HT:PCBM/ PEDOT:PSS (0.5% triton)/ AgNP	0.597	9.40	51.77	2.90
#9	ITO/ PEDOT:PSS/ PBDB-T:ITIC/ PEI-Zn/ E-Ag	0.902	14.30	63.22	8.15
#10	ITO/ PEDOT:PSS/ PBDB-T:ITIC/ PEI-Zn/ AgNP	0.885	14.65	60.47	7.84
#11	ITO/ PEDOT:PSS/ D18-Cl:N3:PCBM/ PEI-Zn/ E-Ag	0.844	26.97	73.95	16.69
#12	ITO/ PEDOT:PSS/ D18-Cl:N3:PCBM/ PEI-Zn/ AgNP	0.815	27.16	68.85	15.23

Reference

S1. J. Natsuki, T. Natsuki and T. Abe, *J. Nanoparticle Res.*, 2013, **15**, 1-8.

S2. F. Guo, P. Kubis, T. Przybilla, E. Spiecker, A. Hollmann, S. Langner, K. Forberich and C. J. Brabec, *Adv. Energy Mater.*, 2015, **5**, 1401779.

S3. S. Berny, N. Blouin, A. Distler, H. J. Egelhaaf, M. Krompiec, A. Lohr, O. R. Lozman, G. E. Morse, L. Nanson, A. Pron, T. Sauermann, N. Seidler, S. Tierney, P. Tiwana, M. Wagner and H. Wilson, *Adv. Sci. (Weinh)*, 2016, **3**, 1500342.

S4. J. Czolk, D. Landerer, M. Koppitz, D. Nass and A. Colsmann, *Adv. Mater. Technol.*, 2016, **1**, 1600184.

S5. M. Koppitz, N. Hesse, D. Landerer, L. Graf von Reventlow, E. Wegner, J. Czolk and A. Colsmann, *Energy Technol.*, 2017, **5**, 1105-1111.

S6. S. Strohm, F. Machui, S. Langner, P. Kubis, N. Gasparini, M. Salvador, I. McCulloch, H. J. Egelhaaf and C. J. Brabec, *Energy Environ. Sci*, 2018, **11**, 2225-2234.

S7. Y. Lin, S. Dong, Z. Li, W. Zheng, J. Yang, A. Liu, W. Cai, F. Liu, Y. Jiang, T. P. Russell, F. Huang, E. Wang and L. Hou, *Nano Energy*, 2018, **46**, 428-435.

S8. Y. Lin, Y. Jin, S. Dong, W. Zheng, J. Yang, A. Liu, F. Liu, Y. Jiang, T. P. Russell, F. Zhang, F. Huang and L. Hou, *Adv. Energy Mater.*, 2018, **8**, 1701942.

S9. A. Liu, W. Zheng, X. Yin, J. Yang, Y. Lin, W. Cai, X. Yu, Q. Liang, Z. He, H. Wu, Y. Li, F. Zhang and L. Hou, *ACS Appl. Mater. Interfaces*, 2019, **11**, 10777-10784.

S10. L. Sun, W. Zeng, C. Xie, L. Hu, X. Dong, F. Qin, W. Wang, T. Liu, X. Jiang, Y. Jiang and Y. Zhou, *Adv. Mater.*, 2020, **32**, e1907840.